

Institute for Computational Mathematics
Hong Kong Baptist University

ICM Research Report
11-01

Dispersion of a cloud of particles by a moving shock: Effects of shape, angle of incidence and aspect ratio

T. B. Dittmann^{*} and G. B. Jacobs[†]

*Department of Aerospace Engineering & Engineering Mechanics,
San Diego State University, San Diego, CA, 92182.*

W. S. Don[‡]

Department of Mathematics, Hong Kong Baptist University, Hong Kong, China.

January 1, 2011

Abstract

This paper discusses the particle-laden flow development of a cloud of particles in the accelerated flow behind a normal moving shock. The effect of aspect ratio of a rectangular and elliptical cloud and the clouds' angle of attack with respect to the carrier flow is studied. Computations are performed with an in-house high-order/high-resolution weighted essentially non-oscillatory (WENO-Z) based Eulerian-Lagrangian solver that solves the conservation equations in the Eulerian frame, while particles are traced in the Lagrangian frame. Streamlined spherical and elliptical clouds exhibit a lower dispersion than blunt rectangular cloud shapes. The averaged and root mean square location of the particle coordinates in the cloud show that with decreasing aspect ratio, the cloud's streamwise convection velocity increases. With increasing rotation the cross-stream dispersion increases if the aspect ratio is larger than unity. The particle-laden flow development of an initially rotated rectangle is qualitatively and quantitatively comparable to the dispersion of an initially triangular cloud.

1 Introduction

Particle-laden and droplet-laden flows play an important role in novel high-speed technologies such as solid rocket propulsion systems and high-speed liquid-fuel combustors. Shock waves, for example, occur in high-speed combustors and interact with fuel particles in the supersonic flow. The trajectories of the fuel droplets determines the dispersion and mixing of the fuel droplets and hence the combustors efficiency. The tremendous physics complexity including shock dynamics, turbulence, particle dynamics, etc. and the large range of scales (from molecular scale to combustors size) have posed the highest demands on both experimental and computational analysis. Experimentally it is difficult to capture all scales, particularly for the fast time scale, while first principle computations are expensive and models not optimal.

In the past two decades, significant effort have gone toward the improvement of empirical governing models for the particle motion through investigation of the acceleration of an individual particle behind a shockwave. Boiko et al.[7] determined the drag of a droplet behind a shock by comparing

^{*}Graduate Student, AIAA student member

[†]Associate Professor, Corresponding author, AIAA member, Email: gjacobs@mail.sdsu.edu

[‡]Professor, Email: wsdon@math.hkbu.edu.hk

the known relaxation times of a hard sphere to their experimentally measured droplet relaxation times. Sun et al.[6] numerically studied the dynamic drag coefficient of a spherical particle behind a shock wave. A reflected bow shock was observed in front of the spherical particle, and as the shock wave traversed over the sphere a Mach reflection formed. The Mach reflection proceeded to the rear center of the sphere before converging with the Mach reflection from the other side. This caused shock focusing to occur and a region of very high pressure at the rear of the spherical particle. This region of high pressure resulted in a brief negative drag. Their numerical data matched experimental data within 10%. Loth[8] investigated the effect of compressibility and rarefaction on a spherical particle. Boiko et al.[5] also studied different shaped particles. In a comparison of a cubical and a spherical particle they found that the drag is predominantly a function of the frontal area of the particle. Therefore the relative bluntness of the shapes did not significantly affect the particle dynamics.

A limited number of studies have been performed on the dynamics of large number of particles in high-speed flow. Olim et al.[2] studied the attenuation of a normal shock wave in a homogeneous gas particle mixture. Kiselev et al.[3] compared simulations based on Boiko’s empirical particle models to shock tube experiments on the dispersion of a cloud of plexiglas and bronze particles in the accelerated flow behind a moving shock[3, 4] . Not only did they visualize the particle dynamics and dispersion, they also matched some of their result quantitatively to the experimental dispersions. In Jacobs et al.[12, 13] , a high-order/high-resolution Eulerian-Lagrangian scheme was developed that was based on the same empirical physical governing model as proposed by Kiselev et al. Extensive high-order/high-resolution results showed good comparison with experimental results, while small scale turbulent structures were resolved with improved efficiency. In Jacobs et al.[12] , we studied the effect of initial shape of the cloud’s geometry on the dispersion of particles. It was shown that the aerodynamics of the shape significantly alter the cross-stream dispersion of particles.

This paper extends the investigation of the effect of the geometry of the cloud on the dispersion of particles in the accelerated flow behind a moving shock. We study the effect of aspect ratio and rotation of the cloud and present detailed statistics of the particle dispersion in terms of the averaged and root mean square particle coordinates. This investigation is part of our ongoing effort to thoroughly validate Eulerian-Lagrangian methods against shock tube experiments for shocked, particle-laden flow.

In Section 2 we present the physical model and the governing equations, and briefly review the high-order/high-resolution Eulerian-Lagrangian method. In Section 3 we first briefly review the effect of particle cloud shape on the dispersion of particles, followed by a discussion of the effect of aspect ratios and rotation of the cloud shapes on the particle-laden flow development. Concluding remarks and future directions are given in Section 4.

2 The Physical Model and Governing Equations

In the particle-source-in-cell (PSIC) method the Eulerian continuum equations are solved for the carrier flow in the Eulerian frame, while particles are traced along in the Lagrangian frame. In the following, we present the coupled system of Euler equations that govern the gas flow and kinematic equations that govern the particle motion. We shall denote the subscript p for the particle variables and f for the gas variables at the particle position. Variables without subscript refer to the gas variables unless specified otherwise. For more detailed discussion of the physical model and governing equations, readers are referred to Ref. [12].

2.1 Euler equation in the Eulerian frame

The governing equations for the carrier flow are the two-dimensional Euler equations in Cartesian coordinates given by:

$$\mathbf{Q}_t + \mathbf{F}_x + \mathbf{G}_y = \mathbf{S}, \quad (1)$$

where

$$\begin{aligned} \mathbf{Q} &= (\rho, \rho u, \rho v, E)^T, \\ \mathbf{F} &= (\rho u, \rho u^2 + P, \rho uv, (E + P)u)^T, \\ \mathbf{G} &= (\rho v, \rho uv, \rho v^2 + P, (E + P)v)^T, \end{aligned} \quad (2)$$

and

$$P = (\gamma - 1) \left(E - \frac{1}{2} \rho (u^2 + v^2) \right), \quad \gamma = 1.4. \quad (3)$$

The equation of state closes the system of equations

$$T = \frac{\gamma P M^2}{\rho}, \quad (4)$$

where $M = U/\sqrt{\gamma RT}$ is a reference Mach number determined with the reference velocity, U and reference temperature, T . The source term, \mathbf{S} , accounts for the effect of the particles on the carrier gas and will be discussed in more detail below.

2.2 Particle equation in the Lagrangian frame

Particles are tracked individually in the Lagrangian frame. The kinematic equation describing the particle's position \vec{x}_p , is given as

$$\frac{d\vec{x}_p}{dt} = \vec{v}_p, \quad (5)$$

where \vec{v}_p is the particle velocity vector.

The particles' acceleration is governed by Newton's second law forced by the drag on the particle. With particles assumed spherical, we take the drag as a combination of the Stokes drag corrected for high Reynolds and Mach number and the pressure drag leading to the following equations governing the particle velocity

$$\frac{d\vec{v}_p}{dt} = f_1 \left(\frac{\vec{v}_f - \vec{v}_p}{\tau_p} \right) - \frac{1}{\rho_p} \nabla P|_f, \quad (6)$$

where \vec{v}_f is the velocity of the gas at the particle position, and ρ_p the particle density. The first term on the right hand side describes the particle acceleration resulting from the velocity difference between the particle and the gas. The second term in the right hand side of (6) represents the particle acceleration induced by the pressure gradient in the carrier flow at the particle position. The particle time constant $\tau_p = Re d_p^2 \rho_p / 18$, where d_p is the particle diameter, is a measure for the reaction time of the particle to the changes in the carrier gas. $Re = UL/\nu$ is the Reynolds number of the carrier gas flow with L a reference length and ν the dynamic viscosity. In this study, we assume Re large and we therefore do not model viscous effects in the governing Eulerian equations for the gas flow (1).

f_1 is an empirical correction factor that yields an accurate determination within 10% of measured particle acceleration for higher relative particle Reynolds number up to $Re_f = |\vec{v}_f - \vec{v}_p|d_p/\nu = 1 \times 10^4$ and relative particle Mach number up to $M_f = |\vec{v}_f - \vec{v}_p|/\sqrt{T_f} = 1.2$ and is given by

$$f_1 = \frac{3}{4} \left(24 + 0.38Re_f + 4\sqrt{Re_f} \right) \left(1 + \exp \left[\frac{-0.43}{M_f^{4.67}} \right] \right). \quad (7)$$

From the first law of thermodynamics and Fourier's law for heat transfer, the equation for temperature is derived as,

$$\frac{dT_p}{dt} = \frac{1}{3} \frac{Nu}{Pr} \left(\frac{T_f - T_p}{\tau_p} \right), \quad (8)$$

where $Pr = 1.4$ is the Prandtl number, taken as its typical value for air in this paper. $Nu = 2 + \sqrt{Re_f Pr}^{0.33}$ is the Nusselt number corrected for high Reynolds number.

2.3 Source term S for the Euler equation

Each particle generates a momentum and energy that affects the carrier flow. The volume averaged summation of all these contributions gives a continuum source contribution on the momentum and energy equation in (1) as:

$$\vec{S}_m(\vec{x}) = \sum_{i=1}^{N_p} \mathbf{K}(\vec{x}_p, \vec{x}) \vec{W}_m, \quad (9)$$

$$S_e(\vec{x}) = \sum_{i=1}^{N_p} \mathbf{K}(\vec{x}_p, \vec{x}) (\vec{W}_m \cdot \vec{v}_p + W_e), \quad (10)$$

where $\mathbf{K}(x, y) = \mathbf{K}(|x - y|)/V$ is a normalized weighing function that distributes the influence of each particle onto the carrier flow. $\vec{W}_m = m_p f_1 (\vec{v}_f - \vec{v}_p) / \tau_p$ and $W_e = m_p (Nu / (3Pr)) (T - T_p) / \tau_p$ are weigh functions describing the momentum and energy contribution of one particle, respectively. m_p is the mass of one spherical particle which can be derived from τ_p . N_p is the total number of particles in an finite volume V .

2.4 Flow and Particle Solver

The governing equations are discretized and solved using the WENO-Z based PSIC scheme as proposed in [12]. The nonlinear nature of the hyperbolic Euler equations admits finite time singularities in the solution even when the initial condition is smooth. It is important that the numerical methods employed avoid non-physical oscillations, also known as the Gibbs phenomenon, when the solution becomes discontinuous. Among many high order shock capturing schemes, the classical weighted essentially non-oscillatory finite difference schemes (WENO) for conservation laws by Balsara et al.[10] has been very successfully employed for the simulation of the fine scale and delicate structures of the physical phenomena related to shock-turbulence interactions

An improved version of classical WENO scheme, namely, WENO-Z scheme[11, 14], is ideally suited for computing a shock wave interacting with a cloud of particles due to the complicated shock structures of the problem, and the importance of preserving high order resolution to resolve the small scale interactions present in particle-laden shocked flow.

The essence of the WENO scheme is the use of adaptive stencils. The method creates a stencil over the computational domain, in which a smoothness indicator is employed to estimate within which

substencils within the stencil the shocks lie. The method then assigns an essentially zero weight to low order interpolation polynomials of the flux based on the values from substencils that contain high gradients and/or shocks to prevent Gibbs oscillations.

In computational cells where there no shock present a high order central difference scheme can be used to calculate the flow properties. But in shocked regions a centered interpolation will produce undesirable Gibbs oscillations. With an ENO interpolation, these oscillations are essentially removed. The ENO interpolation is only necessary in WENO-domains identified by the smoothness indicator. The WENO scheme ensures that the order of accuracy of the simulation remains intact. Once the flow solver updates the flow variables at grid points and their values are used to calculate the flow's influence upon the particles that are located within the computational cell. The particles' influence is also weighted back onto the fluid cell. The interpolation is done with a spline function with the same order of accuracy as the flow solver to avoid excessive computational errors.

3 Results and Discussion

We perform simulation based on the fifth order WENO-Z based PSIC algorithm for flow evolution when a shock runs through a cloud of particles.

To summarize the algorithm, we approximate the system of hyperbolic Euler equations (1) in the Eulerian frame,

$$\frac{d\mathbf{Q}}{dt} = -\nabla \cdot \vec{F}(\mathbf{Q}) + \mathbf{S}(\vec{x}_p - \vec{x}), \quad (11)$$

on each grid point. A N_p number of particles are individually traced in the Lagrangian frame with

$$\frac{d\vec{x}_p}{dt} = \vec{v}_p, \quad (12)$$

$$\frac{d\vec{v}_p}{dt} = f_1 \left(\frac{\vec{v}_f - \vec{v}_p}{\tau_p} \right) - \frac{1}{\rho_p} \nabla P|_f, \quad (13)$$

$$\frac{dT_p}{dt} = \frac{1}{3} \frac{Nu}{Pr} \left(\frac{T_f - T_p}{\tau_p} \right). \quad (14)$$

Interpolation determines \vec{v}_f , and T_f , while weighing determines $\mathbf{S}(\vec{x}_p - \vec{x})$.

We employed the third order Total Variation Diminishing Runge-Kutta scheme (RK-TVD):

$$\begin{aligned} \vec{U}^1 &= \vec{U}^n + \Delta t \mathbf{L}(\vec{U}^n), \\ \vec{U}^2 &= \frac{1}{4} \left(3\vec{U}^n + \vec{U}^1 + \Delta t \mathbf{L}(\vec{U}^1) \right), \\ \vec{U}^{n+1} &= \frac{1}{3} \left(\vec{U}^n + 2\vec{U}^2 + 2\Delta t \mathbf{L}(\vec{U}^2) \right), \end{aligned} \quad (15)$$

where \mathbf{L} is the spatial operator as in the right side of (11) or (14). The CFL number is set to 0.4. We initialize a right running Mach three shock $M_s = 3$ at $x_s = 0.175$ in a rectangular domain $[0, 3] \times [-0.611, 0.611]$. Inflow and outflow boundary conditions are specified, respectively, in the x direction. Periodic boundary conditions are imposed in the y direction. A uniformly distributed bronze particle cloud is seeded in a rectangular shape, $[0.175, 0.352] \times [-0.044, 0.044]$, with zero initial velocity. The volume concentration of the particles in the cloud is 4%. The particle response time and density are, $\tau_p = 51.69$ and $\rho_p = 7.42 \times 10^4$, respectively. We take the Reynolds number needed to compute the particle traces according to the experiment at $Re_f = 3.387 \times 10^7$. In our discussion of the results below, we shall refer to the collection of the particles as *shape*.

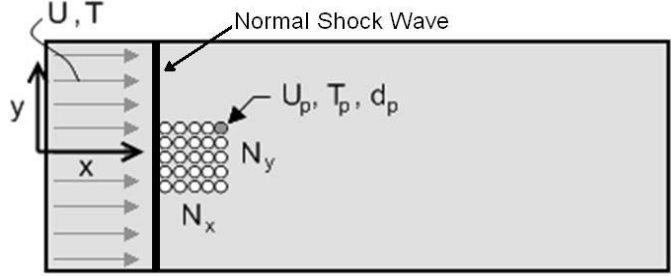


Figure 1: Initial setup of the shock-particle laden flow.

In the following simulations, the number of grid points used to solve the Euler equation in the Eulerian frame is 1500×500 in the x and y directions respectively. The total number of particles is 40K arranged in a 400×100 rectangular shape.

We briefly summarize the effect of initial cloud shape that was studied in Ref. [12] to set the stage for the analysis of the effect of aspect ratio and rotation of the cloud. In Ref. [12], we compared a rectangular, a circular and a triangular cloud shape with the same particle volume concentrations. The clouds covered the same geometric area and are initialized so that the clouds location is right behind the normal shock. At early times the normal shock wave propagates through the particle cloud, and a reflected bow shock forms upstream of the particle cloud (see the vorticity contours in Figure 2). Whereas the bow shock development is comparable for the circular and rectangular cases (Figures 2a and 2b), showing a strong detached bow shock, the more aerodynamic triangular case (Figure 2c) induces a much weaker bow shock.

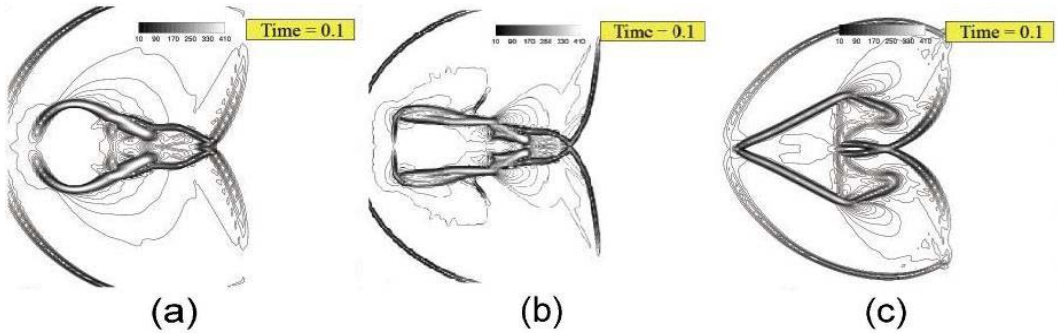


Figure 2: Vorticity contour of the accelerated gas flow behind a moving shock over (a) circular, (b) rectangular and (c) triangular particles cloud shapes at $t = 0.1$.

The gas flow separates at the sharp front corners of the rectangular shape and at the apex of the circular shape. The flow over the triangular shape separates only at the two rear corners. Figures 3a, 3b and 3c show that the particle trajectories closely follow the separated shear layers initially and form distinct material lines. The accelerated flow stagnates at the front of the blunt rectangular and circular cloud shapes compressing these clouds. The particles at the front end move downstream and increase the particle density within the cloud. The leading area of the triangle yields a much lesser compression and the average location of the particles within the cloud do not

move to the right as far as the other two cases. For a more detailed discussion of the effects of shape on this particle-laden flow we refer the reader to Ref. [12].

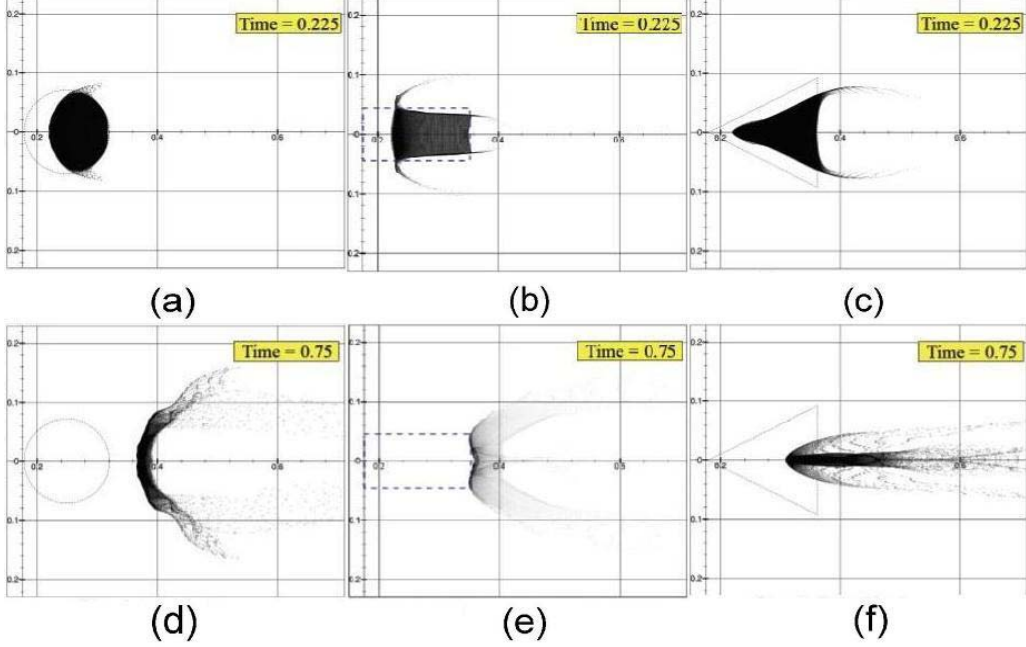


Figure 3: Dispersion pattern of the bronze particles in the accelerated gas flow behind a moving shock over (a, d) circular, (b, e) rectangular and (c, f) triangular particles cloud shapes at $t = 0.25$ and $t = 0.75$.

To quantify the motion and dispersion of the particles we determine the averaged and root-mean-square global statistics on the particle cloud. The mean x -displacement of the particles $x_{disp}(t)$ is determined by comparing the particles average location at time t , $\bar{x}(t)$, to their average location at the initial time $t = 0$, $\bar{x}(0)$ and the dispersion in cross-streamwise y -direction $y_{disp}(t)$ is determined by the root-mean-square deviation from the average y -location of the cloud $\bar{y}(t)$ at time t , namely,

$$x_{disp}(t) = \bar{x}(t) - \bar{x}(0), \quad (16)$$

$$y_{disp}(t) = \sqrt{\frac{1}{N_p} \sum_{i=1}^{N_p} (y_{p,i}(t) - \bar{y}(t))^2}, \quad (17)$$

where

$$\bar{x}(t) = \frac{1}{N_p} \sum_{i=1}^{N_p} x_{p,i}(t), \quad \bar{y}(t) = \frac{1}{N_p} \sum_{i=1}^{N_p} y_{p,i}(t),$$

are the averaged x -location and y -location of N_p number of particles at time t , respectively. The left figure in Figure 4, the temporal evolution of $x_{disp}(t)$ statistic shows that the circular and the rectangular cloud have a comparable movement in x -directions, while the triangles motion is 40% less. The difference is attributed to the smaller force between the gas and particle phase in x -direction induced by the more aerodynamic triangle. A smaller force translates to a lesser acceleration of the shape in x -direction according to Newton's second law.

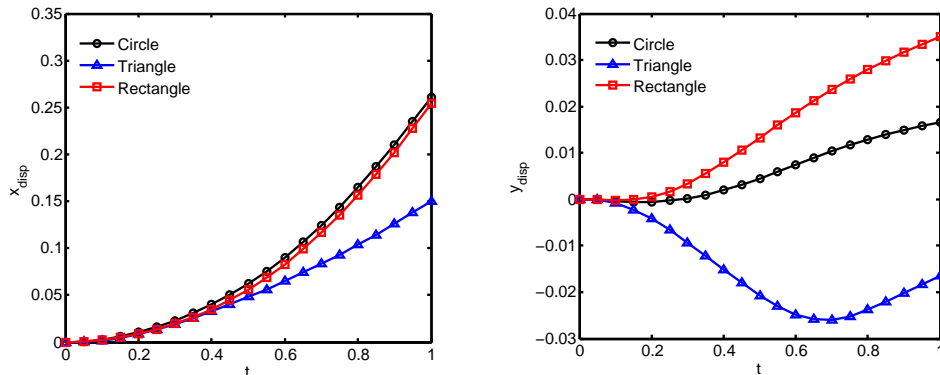


Figure 4: Temporal history of (Left) the averaged x -location $x_{disp}(t)$ and (Right) the root-mean-square y -location deviation $y_{disp}(t)$ of the circular, rectangular and triangular cloud shapes.

The right figure in Figure 4, the temporal evolution of $y_{disp}(t)$ statistic shows that the particle transport along separated shear layers at the front corners of the rectangle induces the greatest dispersion of particles in cross-stream as compared to the other shapes. While from a comparison of the particle snapshots in Figures 3a and 3b it would appear that the circle shape leads to a larger dispersion in cross-stream as compared to the rectangle, the y_{disp} in Figure 4 shows that most particles in the circle shape stay near the symmetry line and dispersion is less. The relative motion of particles in the triangular shape in time is greater than those in the circle and the rectangle. However, the compression of the triangle cloud in time, as shown in Figures 3c and 3f, causes y_{disp} to be negative and hence the dispersion of the cloud is significantly reduced for the triangle as compared to the other shapes.

3.1 Effect of Aspect Ratio η

Changing the cloud's aspect ratio, η , defined as the ratio of the length of the initial cloud shape in x -direction to the width of the initial cloud shape in y -direction, does not change the qualitative behavior of the particle-laden flow dynamics for a given type of shape at early ($t < 0.4$) and later times ($t > 0.7$).

The snapshots of velocity magnitude contours, streamlines and particles in Figure 5 at time $t = 0.3$ and $t = 1$ that, the particles in the rectangular cloud are transported along the separated shear layers at the front and rear corners of the shape at early times. At later time the arms that have formed at front corners shield the flow extending the width of the wake. The reduced velocity in the wake prevents further transport of the particles into the arms at the rear corners of the shape. The flow separation location changes with time along the smooth surface of the ellipsoidal shapes. Like for the rectangular shape, particles are transported along the separated shear layers. Since the separated location is moving in time as opposed to the fixed separation at the front corners of the rectangular cloud shapes, the particle arms are less defined for the ellipsoidal shapes at early times.

Both circular and rectangular clouds with $\eta > 1$ are compressed relatively more in x -direction in time than clouds with $\eta < 1$. Clouds with $\eta < 1$ experience more compression along the longer sides in y -direction as compared to clouds with $\eta > 1$ that have relatively small lengths along the sides.

With an increase of the cloud's aspect ratio, the cloud's geometry is more slender and the cloud

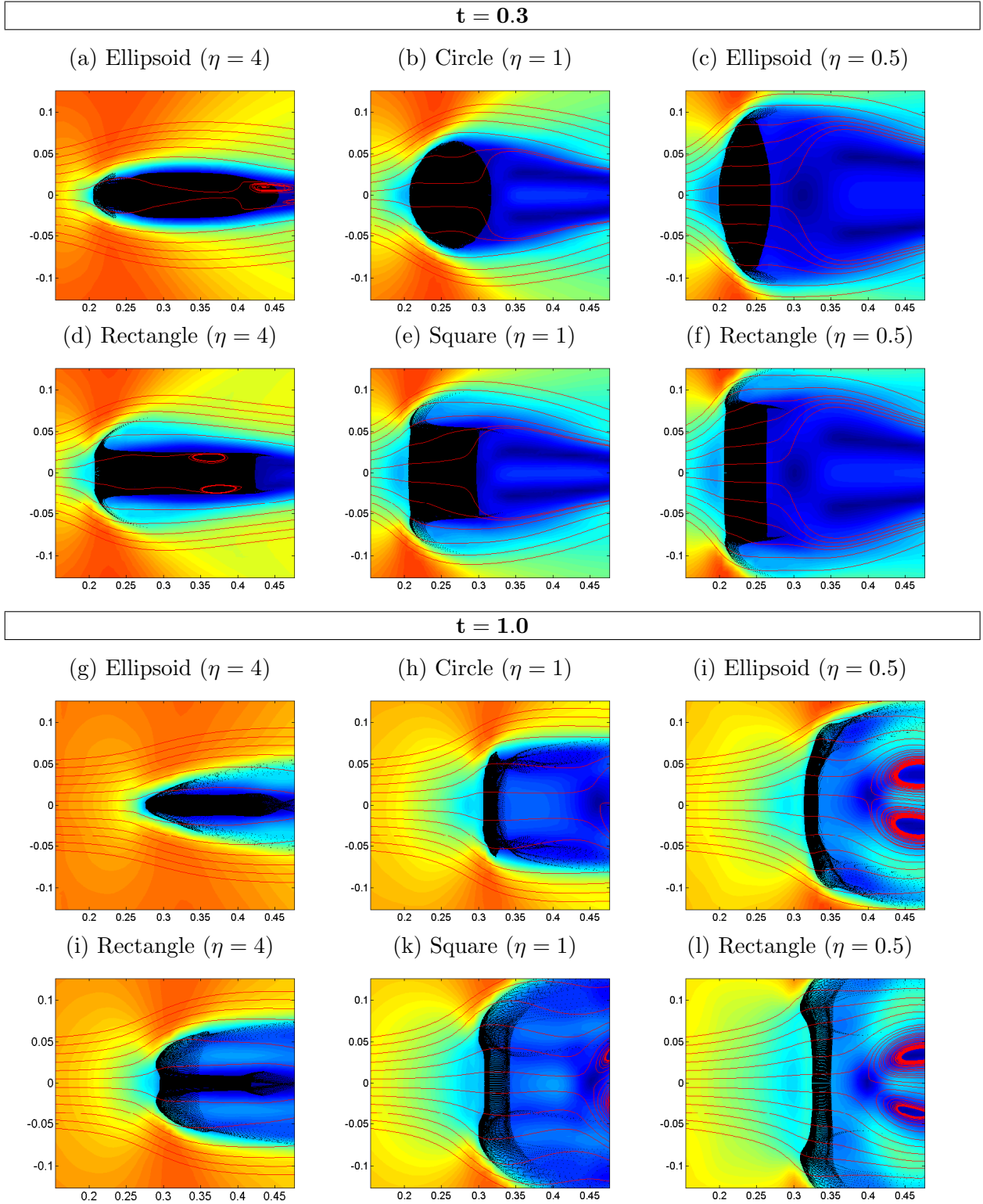


Figure 5: Velocity magnitude contours, streamlines and particles for (a,g) ellipsoid with $\eta = 4$, (b,h) circle with $\eta = 1$, (c,i) ellipsoid with $\eta = 0.5$, (d,j) rectangle with $\eta = 4$, (e,k) square with $\eta = 1$, and (f,l) rectangle with $\eta = 0.5$, at time $t = 0.3$ and $t = 1.0$, respectively.

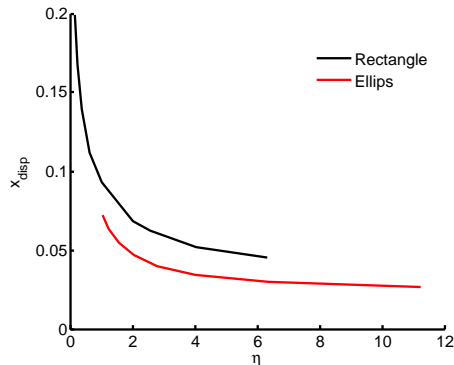


Figure 6: $x_{disp}(t)$ versus aspect ratio η , for initially rectangular and ellipsoidal particle clouds at $t = 1$.

obstructs the flow less. For higher aspect ratio η , the wake zones and low velocity stagnation areas in front of the shape are hence decreasing. The slender geometry is inducing a smaller forcing between the gas and particle phase, which results in the reduced convection of the cloud in x -direction with increased η , as shown in Figure 5, for both the ellipsoidal and rectangular shape at late time $t = 1$. The reduced convection of the ellipsoids as compared to the rectangles, shows that ellipsoid induces a smaller mutual forcing and is more aerodynamic.

3.2 Effect of Rotation θ

To rotate the shape we change the coordinates of particles in the rectangle and the ellipsoids as follows

$$[x_p, y_p]_{new} = \mathbf{R}[x_p, y_p]_{old}, \quad (18)$$

where

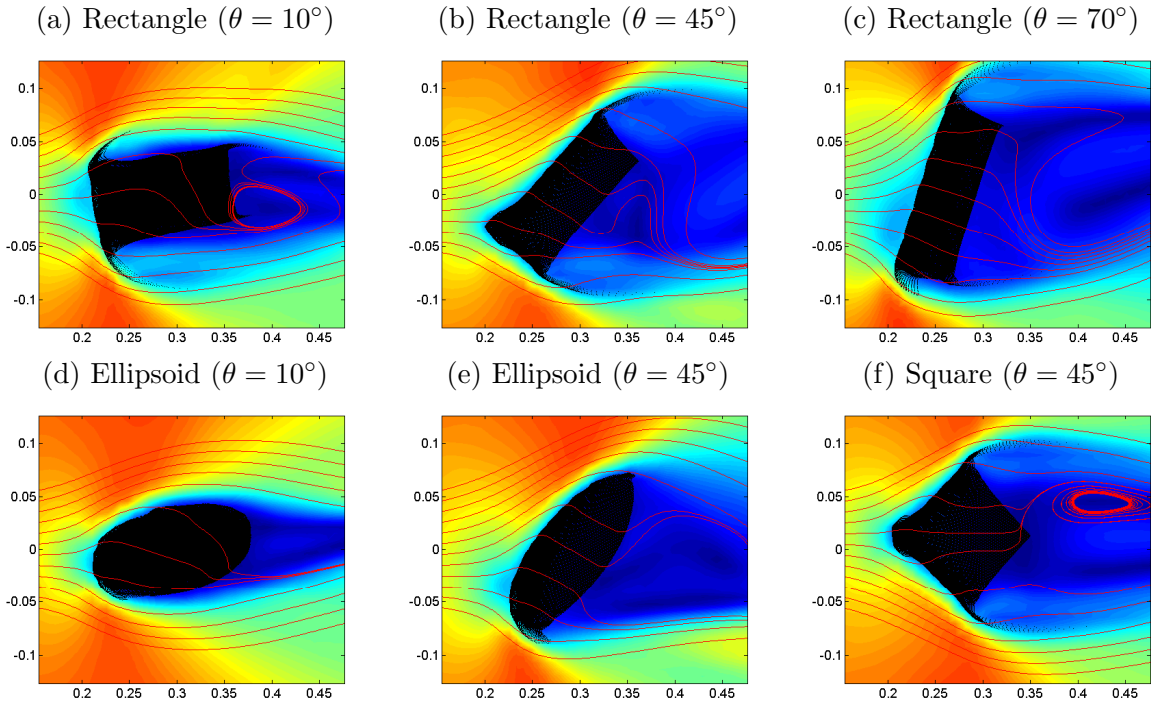
$$\mathbf{R} = \begin{bmatrix} \cos \theta & -\sin \theta \\ \sin \theta & \cos \theta \end{bmatrix}, \quad (19)$$

is the rotation matrix with a given angle of rotation θ . The leading point of the rotated particle cloud is initially positioned right behind the right moving shock at $x = 0.175$ ensuring that the shock wave moves through the cloud at the same time for all rotation angles.

Snapshots of the velocity magnitude and particles at early time (Figures 7a and 7d) show that the particle-laden flow developments are similar at moderate angles of attack as compared to the flow developments of the shapes at zero angle of rotation. Particles separate into arms along the front corner of the rectangle at early times and shield the flow from the trailing part of the cloud at later times. However, the flow strength, flow separation and particle arm at the bottom front corner are larger at the top front corner as compared to the bottom corner at angles of rotation. Since the larger arm shields the rear of the rectangle more on the bottom than on the top, the particle arm that initially formed at the top rear corner is more exposed to the incoming flow and hence is larger at later times (Figures 7g and 7j). The ellipsoid shape shows similar asymmetries in the separated particle arms and gas flow at early and late times at moderate angle of rotation.

As the angle of rotation θ further increases, the particle-laden flow development dramatically changes both qualitatively and quantitatively. At medium angles of rotation the flow development of the initially rectangular cloud is showing similar features to the flow development of the

t = 0.3



t = 1.0

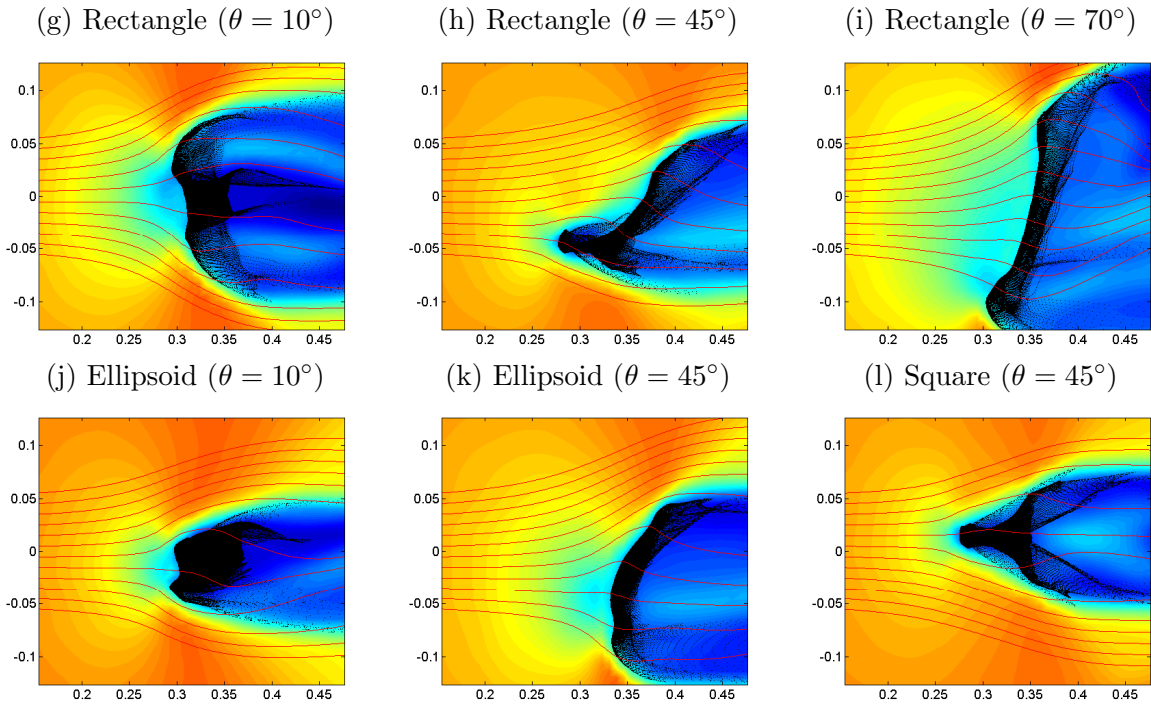


Figure 7: Velocity magnitude contours, streamlines and particles for cloud shapes with a fixed aspect ratio $\eta = 2$ for (a,g) rectangle with $\theta = 10^\circ$, (b,h) rectangle with $\theta = 45^\circ$, (c,i) rectangle with $\theta = 70^\circ$, (d,j) ellipsoid with $\theta = 10^\circ$, (e,k) ellipsoid with $\theta = 45^\circ$, and (f,l) square with $\theta = 45^\circ$, at time $t = 0.3$ and $t = 1.0$, respectively.

initially triangular particle cloud (Figures 6b and 7b). One of the front corners of the shape now protrudes into the flow and the flow does not separate from this corner. Since the flow is attached along the sides, particles no longer leave from the shape at this corner. At early times most particles are transported out of the shape at the two corners that are downstream of the leading corner of the rectangle comparable to particle dynamics of the triangular cloud. At later times the rectangular shape has been compressed towards the symmetry line, also comparable to the triangle case (Figure 7h). The ellipsoidal case is very similar to the rectangular case at medium angle of rotation (Figures 7d and 7j), but the smoother geometry leads to particles arms and flow separations that are less distinct.

We note that the case of a rectangle with $\eta > 1$ and large angle of rotation (Figure 7c and 7i) is geometrically the same as a rectangle with $1/\eta$ with small angle of rotation. As discussed previously, the particle-laden flow developments of shapes with small rotation angle are comparable to the flow developments of the same shape with zero angle of rotation.

To underscore that the flow dynamics of a rectangle cloud at medium angles are comparable to that of a triangle, we place a square ($\eta = 1$) under angle of rotation $\theta = 45^\circ$. The front half of the diamond shape is now geometrically exactly a triangle. From the snapshots at early time (Figure 7f) and late time (Figure 7l), we can see that the dynamics of this front half are indeed the same as that of the triangle described above. The trailing half of the diamond does not move significantly and since this half is shielded from the oncoming flow it does not significantly affect the gas flow either at early times. At later times, the wider trailing half of the diamond is exposed to the oncoming flow yielding a slightly wider cloud and wake as compared to the triangle case.

The square cloud is convected further downstream in x -direction at zero angle of rotation $\theta = 0^\circ$ than at $\theta = 45^\circ$ of rotation (when it behaves like a triangle), since the force between gas and particle phase is larger for the blunt square shape at zero rotation as compared to the more aerodynamic rotated shape. The averaged x -location of the cloud, x_{disp} , is hence larger at small angle of rotation as compared to medium angles of rotation (Figure 7g). Because of the square's symmetry, the x_{disp} curve is symmetric versus angle of rotation θ .

Noting again that a shape with $\eta > 1$ at ninety degree of rotation ($\theta = 90^\circ$) is geometrically the same as that same shape with $1/\eta$ at $\theta = 0^\circ$, it follows that x_{disp} is smaller for $\eta > 1$ at $\theta = 0^\circ$ as compared to that shape at $\theta = 90^\circ$, similar to the trends of x_{disp} versus η in Figure 6. We observe that curves for different aspect ratio in Figure 8a cross through a single point, indicating a correlation between rectangular shapes at a rotation angle $\theta \approx 25^\circ$.

At medium rotation rectangles behave like triangles and hence they show a minimum y_{disp} for all η (Fig. 8b). The minimum is naturally at $\theta = 45^\circ$ for the symmetric square and the angle at which y_{disp} has a minimum reduces with increasing η .

A comparison of x_{disp} for the ellipsoid cloud in Figure 9 with x_{disp} for the rectangular cloud in Figure 8a confirms the similarity between the two shapes. The trends with rotation and aspect ratio are the same and Figure 9 shows the same crossing at a single point of the curves with different aspect ratio, only at a slightly larger rotation angle of $\theta = 30^\circ$. Note that since a circle with $\eta = 1$ does not change geometrically with rotation, x_{disp} of an ellipsoid is not affected by rotation at $\eta = 1$.

4 Conclusions and Future Developments

A numerical study using a high-order/high-resolution Eulerian-Lagrangian method on the effect of initial shape, aspect ratio and rotation of a cloud of particles on the particle-laden flow development in the accelerated flow behind a moving shock is conducted.

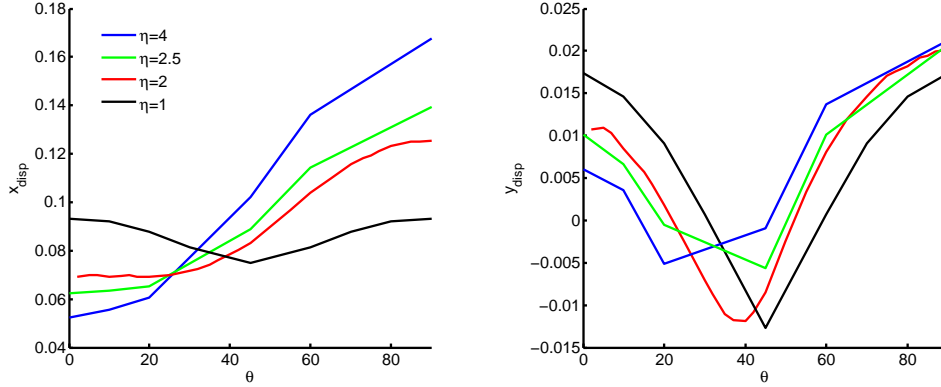


Figure 8: (a) $x_{disp}(t)$ and (b) $y_{disp}(t)$ versus angle of rotation, θ , for initially rectangular particle clouds with aspect ratio $\eta = 1, \dots, 4$.

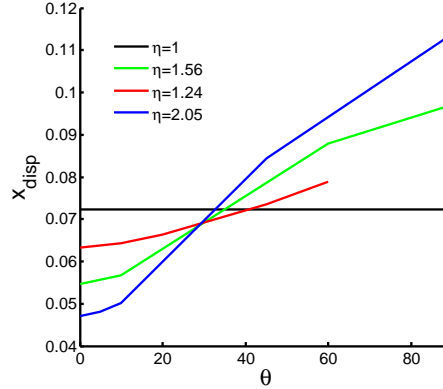


Figure 9: $x_{disp}(t)$ versus angle of rotation θ , for initially ellipsoidal particle clouds with aspect ratio $\eta = 1, \dots, 2.05$.

A change of shape dramatically changes the particle-laden flow development. In the case of initially rectangular cloud shape, particles separate mostly along separated shear layers into distinct arms that emanate from the front corners. These arms shield the incoming flow from the rear part of the cloud. The flow separation location is changing in time along the smooth circle cloud surface, and hence the particle arms are less distinct as compared to the initial rectangular cloud. The flow remains attached along the sides of the more aerodynamically shaped triangular cloud. Particles are transported along shear layers that emanate from the rear corners.

The averaged triangular cloud location is convected 40% less downstream as compared to the blunt rectangular and the circular cloud. This is attributed to a reduced forcing and hence acceleration between gas and particle phase for the aerodynamic triangle shape. The attached gas flow along the side of triangle compresses particles towards the symmetry line, leading to a reduction of the root-mean-square cross-stream location of the cloud particles. The particles that are pulled out of the rectangular and circular shapes by separated shear layers move away from the symmetry line and increase the root-mean-square cross-stream cloud location.

A change of aspect ratio does not change the particle-laden flow qualitatively. However, a slender, aerodynamic high aspect ratio shape is convected more in streamwise direction as compared to low

aspect ratio shapes. Low aspect ratio shapes are relatively more compressed in streamwise direction, whereas high-aspect ratio shapes are relatively more compressed in cross-stream direction.

Except for small wake and dispersion asymmetries, at small angle of rotation, qualitative flow developments are similar to the case of zero angle of rotation. At medium angles of rotation, the flow characteristics of the cases with rectangular and ellipsoidal clouds are comparable to the flow features of the initially triangular cloud case.

The current investigation is part of a larger effort to validate our high-order/high-resolution Eulerian-Lagrangian solver against shock-tube experiments of a particle cloud dispersion in the flow behind a moving shock. Results are databased, while the particle-laden shocked flow developments are elucidated and documented. We have extended our codes to three-dimensions recently and are conducting investigations into the three-dimensional effects on these configurations.

5 Acknowledgments

We gratefully acknowledge the support of this work by AFOSR contract No. G00008044 and the California Space Grant Consortium. The third author (Don) also would like to thank the support provided by the Earmarked Research Grant HKBU-200909 from the Research Grants Council of Hong Kong.

References

- [1] C. T. Crowe, M. P. Sharma and D. E. Stock, *The Particle-Source in Cell (PSI-Cell) Model for Gas-Droplet Flows*, J. Fluids Eng. **6**, pp. 325–332 (1977)
- [2] M. Olim, G. Ben-Dor, M. Mond, O. Igra, *A General Attenuation Law of Moderate Planar Waves Propagating into Dusty Gases with Relatively High Loading Ratios of Solid Particles*, Fluid Dynamics Research **6**, pp. 185–199 (1990)
- [3] V. Kiselev, S. Kiselev and V. Fomin, *Interaction of a Shock Wave with a Cloud of Particles of Finite Dimensions*, J. Appl. Mech. and Tech. Phys. **35**, pp. 183–192 (1994)
- [4] V. Boiko, V. Kiselev, S. Kiselev, A. Papyrin and S. Poplavskii, *Interaction of a Shock Wave with a Cloud of Particles*, Combustion, Explosion, and Shock Waves **32**, pp. 191–203 (1996)
- [5] V. Boiko and S. Poplavsky, *Dynamics of Irregularly Shaped Bodies in a Flow Behind a Shock Wave*, C. R. Mecanique **332**, 2004, pp. 181–187 (2004)
- [6] M. Sun, T. Saito, K. Takayama and H. Tanno, *Unsteady Drag on a Sphere by Shock Wave Loading*, Shock Waves **14**, pp. 3–9 (2004)
- [7] V. Boiko and S. Poplavsky, *Particle and Drop Dynamics in the Flow behind a Shock Wave,* Fluid Dynamics, Fluid Dynamics **42**, pp. 441–443 (2007)
- [8] E. Loth, *Compressibility and Rarefaction Effects on Drag of a Spherical Particle*, AIAA Journal **46**, pp. 2219–2228 (2008)
- [9] M. Tate, Im. Kyoung-Su and C. Seong-Kyun, *Interaction Between a Supersonic Disintegrating Liquid Jets and Their Shock Waves*, Phys. Rev. Let. **102** (2009)
- [10] D. Balsara and C. W. Shu, *Monotonicity Preserving Weighted Essentially Non-Oscillatory Schemes with Increasingly High Order of Accuracy*, J. Comp. Phys. **160**, pp. 405–452 (2000)

- [11] R. Borges, M. Carmona, B. Costa and W. S. Don, *An Improved Weighted Essentially Non-Oscillatory Scheme for Hyperbolic Conservation Laws*, J. Comp. Phys. **227** No. 6, pp. 3101–3211 (2008)
- [12] G. Jacobs and W. S. Don, *A High-Order WENO-Z Finite Difference based Particle-Source-in-Cell Method for Computation of Particle-Laden Flows with Shocks*, J. Comp. Phys. **228** No. 5, pp. 1365–1379 (2009)
- [13] G. Jacobs, W. S. Don and T. Dittmann, *High-Order Resolution Eulerian-Lagrangian Simulations of Particle Dispersion in the Accelerated Flow behind a Moving Shock*, Theor. Comput. Fluid Dyn., DOI 10.1007/s00162-010-0214-6
- [14] M. Castro, B. Costa and W. S. Don, *High Order Weighted Essentially Non-Oscillatory WENO-Z schemes for Hyperbolic Conservation Laws*, J. Comp. Phys., ISSN 0021-9991, DOI: 10.1016/j.jcp.2010.11.028